PROCEEDINGS, 41st Workshop on Geothermal Reservoir Engineering
Stanford University, Stanford, California, February 22-24, 2016
SGP-TR-209

Sources of Subsidence at the Salton Sea Geothermal Field

Andrew J. Barbour[1], Eileen L. Evans[1], Stephen H. Hickman[1] and Mariana Eneva[2]

1 - U.S. Geological Survey, Menlo Park, CA, USA

2 - Imageair Inc., Reno, NV, USA

abarbour@usgs.gov

Keywords: Salton Sea Geothermal Field, InSAR, subsidence, poroelasticity

ABSTRACT

At the Salton Sea Geothermal Field (SSGF) in Southern California, surface deformation associated with geologic processes including sediment compaction, tectonic strain, and fault slip may be augmented by energy production activities. Separating the relative contributions from natural and anthropogenic sources is especially important at the SSGF, which sits at the apex of a complex tectonic transition zone connecting the southern San Andreas Fault with the Imperial Fault; but this has been a challenging task so far. Here we analyze vertical surface velocities obtained from the persistent scatterer InSAR method and find that two of the largest subsidence anomalies can be represented by a set of volumetric strain nuclei at depths comparable to geothermal well completion zones. In contrast, the rates needed to achieve an adequate fit to the magnitudes of subsidence are almost an order of magnitude greater than rates reported for annual changes in aggregate net-production volume, suggesting that the physical mechanism responsible for subsidence at the SSGF is a complicated interplay between natural and anthropogenic sources.

1. INTRODUCTION

Subsidence is a phenomenon common to industrial development of geothermal energy fields, where in most cases only a fraction of the volume of water or steam extracted from the reservoir is re-injected, which induces localized volumetric strain changes. An extreme case is the Wairakei–Tauhara field in New Zealand, where recent subsidence rates are on the order of 100 mm yr^{-1} over an area of <10 km^2, and peak rates have been nearly five times that prior to subsidence-mitigation efforts (e.g., Allis, et al., 2009). Even though deformation associated with focused subsidence can be measured with high accuracy using geodetic methods, it is difficult to quantify the relative contribution from geothermal activities at locations where surface deformation is also influenced by geologic processes such as sediment compaction, and seismic or aseismic fault slip.

The Salton Sea Geothermal Field (SSGF) is an example where separating natural and anthropogenic sources of subsidence is indeed difficult. Located at the southern end of the Salton Sea, in southern California, the SSGF represents the second largest producer of geothermal energy in the state, behind The Geysers, and utilizes only a fraction of the available resource potential (Klein et al., 2004). The SSGF is also located at a tectonic transition zone between the San Andreas and Imperial faults, characterized by a complex pattern of transtensional deformation (e.g., Brothers et al., 2009) and intense seismicity (e.g., Shearer et al., 2005); this is known as the Brawley Seismic Zone (BSZ; Figure 1). Surface deformation at the SSGF represents a mixture of signals from sediment compaction, and seismic and aseismic fault slip (e.g., Lohman and McGuire, 2007), and possibly production-related effects. However, it has been difficult to separate these signals because spatially dense geodetic surface deformation estimates are difficult to obtain: agricultural activities in the area create a paucity of stable monuments to either deploy Global Positioning System (GPS) measurements at (e.g., Crowell et al., 2013), or for radar interferometry (InSAR) (e.g., Wei and Sandwell, 2010).

Despite these complications it is important to quantify the various contributions to the observed deformation field in order to improve assessments of possible triggering hazards at the southern San Andreas Fault (SAF) (e.g., Brothers et al., 2011). Radar data from *Eneva et al.* (2012) show a spatially coherent pattern of subsidence at the SSGF, with a peak rate of nearly 32 mm yr^{-1} greater than background rate – a rate comparable to the magnitude of the relative velocity between the Pacific and North American Plates (Figure 1), for example. *Barbour et al.* (2016) study these velocity estimates in detail, finding that fault slip cannot account for the magnitude and spatial details of the surface deformation; rather, the best agreement comes from a simple model of volumetric strain in a homogeneous poroelastic medium, and they propose that the observed surface velocity anomalies at the SSGF are dominated by strains induced by depletion of the geothermal reservoir. Since ~1989 the SSGF has re-injected roughly 80% of the reservoir brine produced. In this paper we explore a new set of modeling scenarios to test the hypothesis that depletion of the reservoir varies in space, rather than being focused at a single location.

2. MEASURED SUBSIDENCE AT THE SSGF

Eneva et al. (2012) applied the persistent scatterer InSAR (PS-InSAR) method to ascending and descending radar acquisitions from the Envisat satellite between 2003 and 2010, revealing two major anomalies in the relative vertical velocity field at the SSGF corroborated by TerraSAR-X data and leveling surveys. The spatial details of the PS-InSAR anomalies resemble a pattern expected for declining pressures in an idealized fluid reservoir (e.g., Geertsma, 1973; Segall, 1985); however, complex tectonics at the southern end of the Salton Sea suggest that natural causes might also be important. The present paper attempts to differentiate between anthropogenic and natural subsidence in the SSGF.

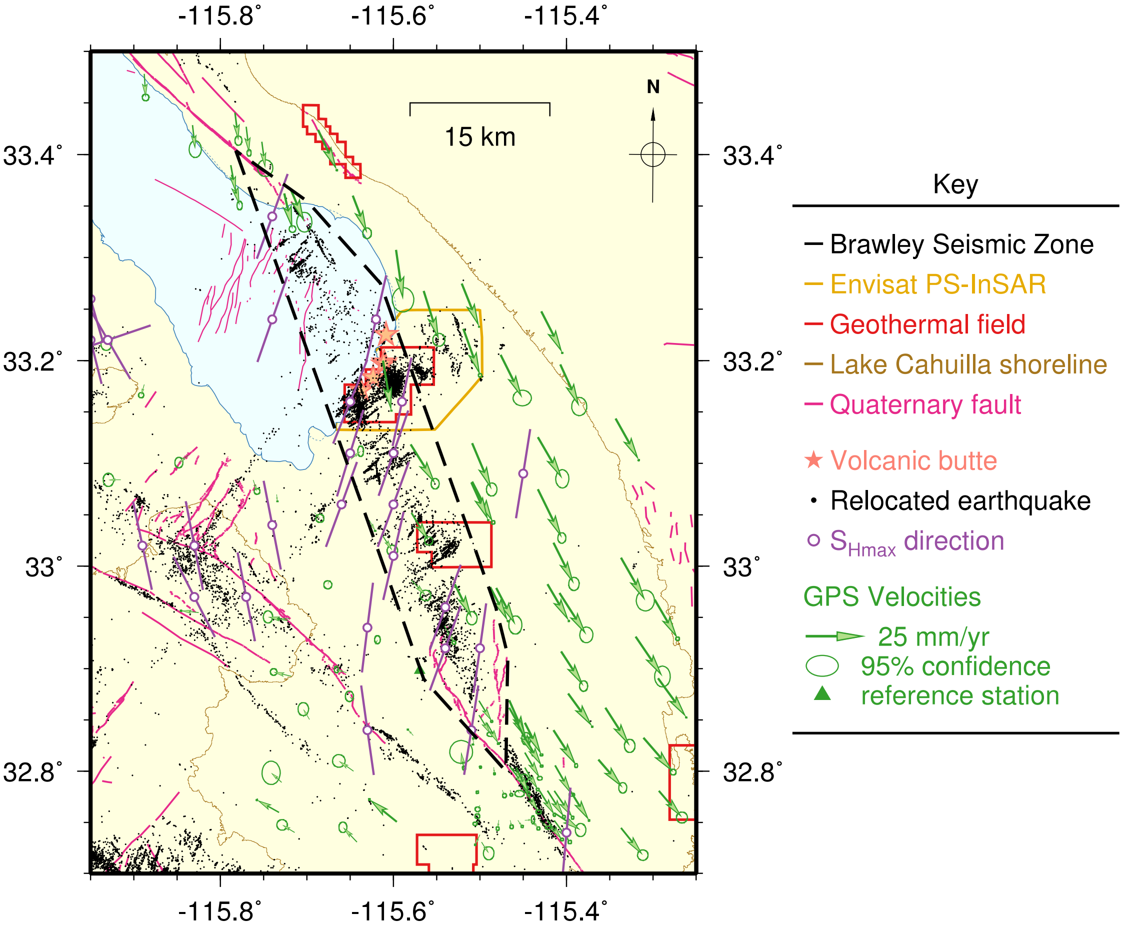

Figure 1: Features in the Brawley Seismic Zone in Southern California, a transition between the southern San Andreas Fault and the northern Imperial Fault. The Salton Sea Geothermal Field is located within the polygon showing the extent of Envisat PS-InSAR data (Eneva et al., 2012) used in this study (Figure 3). Maximum compressive-stress orientations (bars) are from focal mechanism inversions (World Stress Map), horizontal GPS velocities (arrows) are from *Crowell et al.* (2013), and relocated earthquakes (dots) are from *Yang, Haukkson, and Shearer* (2012).

When the relative PS-InSAR velocity estimates are tied to independent estimates of vertical velocity at the nearest continuous GPS station (P507) at a local volcanic outcrop, Red Hill, the absolute rate of ground subsidence reaches ~ 42 mm yr^{-1} and ~ 52 mm yr^{-1} at the center of the two respective subsidence anomalies (see Figure 3A). Whereas the larger anomaly is located between a cluster of injection wells and a cluster of production wells, the smaller anomaly is coincident with wellheads for Vonderahe 1 (Calif. API 025-90633) and Sinclair 10 (Calif. API 025-90871) – Vonderahe 1 is the largest producer of both energy and fluid mass in the entire field.

3. SOURCES OF SUBSIDENCE

From a simplified perspective, the set of plausible mechanism(s) explaining the high rates of focused subsidence at the southern end of the Salton Sea include

1. Sediment compaction and diagenesis
2. Seismic or aseismic moment release (fault slip)
3. Cooling of recent magmatic intrusions
4. Thermoelastic effects from geothermal energy production at the SSGF
5. Poroelastic effects from production-induced fluid losses at the SSGF

Any combination of sources 1 – 5 could contribute to the total observed field at the surface, and here we outline reasons why some of these mechanisms are unlikely.

3.1 Sediment compaction and diagenesis

At the SSGF and elsewhere in the Salton Trough, continental crust is overlain by nearly 6 km of sedimentary material, at various stages of metamorphism (Younker et al., 1982). The sedimentation depocenter, where fluxes are greatest, is beneath the Salton Sea at its southern end (Brothers et al., 2009). As sediment is deposited the material undergoes an inelastic reduction in pore-space by chemical and mechanical processes, causing uniform vertical strain and displacement of the deposition surface, and either a loss of pore fluid or, if the material is undrained, an increase in pore pressure at depth. At depths less than a few kilometers the dominant mechanism will be mechanical compaction, for which the associated subsidence depends largely on the accumulation rate, material density, and fluid saturation of the sedimentary material.

Compaction rates in deltaic plains, for example, are not much larger than a few millimeters per year (Meckel, ten Brink, and Williams, 2007), but these do not account for plasticity effects associated with diagenesis. In a high temperature environment, diagenesis will contribute to pore space collapse where thermal gradients are largest, at depths less than 600 m to 700 m in the SSGF. Even though thermal gradients vary across the SSGF field, there is little evidence (Younker, et al., 1982) for the existence of short-wavelength variations needed – less than a few km across – to explain the focused subsidence.

Assuming steady rates of homogeneous sedimentation flux, the depth profile of porosity, $\varphi(z)$, depends on the porosity of the material at the deposition surface, $\varphi_0 \equiv \varphi(z=0)$, and the effective stress (lithostatic stress minus pore pressure) in the rock, $\sigma'(z)$; to first-order accuracy this relationship (known as Athy's law) for a fluid-saturated porous medium is expressed (Smith, 1971) as $\varphi(z) = \varphi_0 e^{-\beta\,\sigma'(z)}$, where β is the compressibility of the solid matrix. Porosity changes inferred from this model applied to shale layers in the Gulf of Mexico, for example, are consistent with $\varphi_0 = 0.386$ and $\beta = 0.0313$ MPa^{-1} (Zoback, 2010). Even though compaction processes are certainly responsible for some proportion of the background subsidence rate, sediment deposition is relatively uniform across the basin, as is reflected in conceptual models of the reservoir and thermal cap (e.g., Hulen et al., 2002). Again, there would need to be lenses of material having both strong differences in density and/or porosity and spatial dimensions needed to produce focused subsidence.

3.2 Moment release

Slip on high-angle normal faults is a strong candidate for explaining the observed subsidence. *Barbour et al.* (2016) explore the possibility that subsidence in the PS-InSAR is due entirely to (a) slip on two major fault structures cutting across the SSGF (i.e., the faults in Lohman and McGuire, 2007; and McGuire et al., 2015), and (b) coseismic moment release from the observed seismicity. They find that neither possibility is a sufficient mechanism for generating the observed surface deformation rates. Besides the unacceptably high levels of misfit between models and observations, their test results show either unphysical slip rates [in the case of (a)] or small effects at the surface [in the case of (b)], and poor spatial agreement (in both cases). The observed deformation cannot be attributed to cumulative strain from seismic moment release assuming a crustal shear modulus of 10 GPa (Figure 2), implying that most of the observed deformation must be from aseismic deformation.

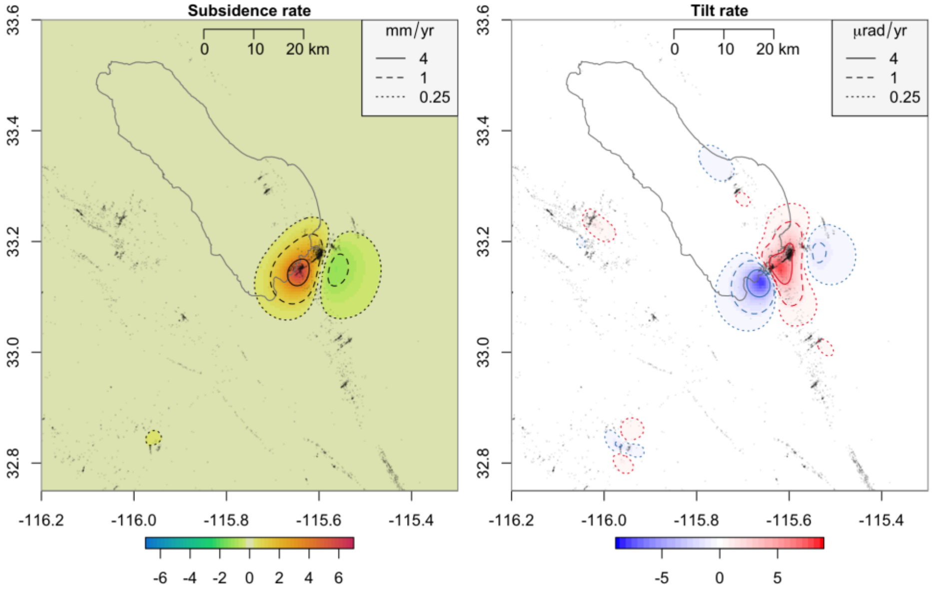

Figure 2: Subsidence and tilt rates associated with seismic moment release from 2003 to 2010, calculated from double-couple mechanisms (Yang et al., 2012) in an elastic halfspace (Okada, 1985). The largest contribution to surface deformation comes from the M5.1 mainshock of the 2005 Obsidian Butte seismic swarm (e.g., Lohman and McGuire, 2007).

It could be the case that crustal faults in this region are much smaller and more pervasive than considered here. However, given that the largest earthquake measured near the SSGF since production began is the 2005 **M**5.1, which was preceded by an aseismic slip transient equivalent to **M**5.7 (Lohman and McGuire, 2007), crustal scale faults accommodating distributed tectonic strain across the BSZ are likely much longer (> 20 km) than the predominant wavelengths seen in the PS-InSAR subsidence anomalies (< 5 km). The slip rates required to explain the observed subsidence with a set of small-scale faults would need to be much larger than rates on faults below the Salton Sea, which paleoseismic evidence indicates are the most active in the region (Brothers et al, 2009). Detailed fault maps with estimates of slip-rate are needed to investigate this further, since most of the faults imaged by McGuire et al. (2015) are active in the shallow crust (< 1 km depths).

Although we may expect some contribution to subsidence from the motion of crustal blocks, there is a lack of surface expression of faults in the Salton Trough except during triggered slip episodes (e.g., Rymer et al., 2011), indicating that slip rates on any of the buried faults in the BSZ must be equal to or less than the greatest sediment accumulation rate. At the offshore depocenter, sediment accumulation rates are somewhere between 10 and 20 mm yr^{-1} (Brothers et al., 2009), but rates elsewhere in the region are only a few mm yr^{-1} (Van De Kamp, 1973), which places strong geologic-based upper bounds on long-term slip rates in the BSZ. Wright et al., (2015) study the eruption history of the volcanic buttes at the southern Salton Sea, and infer a sedimentation rate of 8 – 9 mm yr^{-1} based on shallow drill holes near Obsidian Butte. Furthermore, borehole logs from the SSGF indicate that reservoir cap rock (between 80 m and 300 m depths) is intact across much of the field, showing no significant fault-related offsets (Hulen et al., 2003), which indicates that hydrothermal sealing of the clay-rich cap rock is rapid compared to fault slip rates.

3.3 Magmatic sources

Crystallization and cooling of magmatic bodies could be the source of ongoing thermoelastic strain, leading to subsidence at the surface. *Hulen and Pulka* (2001) document a pair of extrusive rhyolites similar in composition to the Salton Buttes (e.g., Obsidian Butte) within the geothermal reservoir, buried at ~1.6 km with a thickness of 150–300 m and limited lateral extent. According to the mapped locations of these volcanic bodies, it may be possible that they contribute to the largest subsidence anomaly in the PS-InSAR data, but these bodies appear to be fully cooled. Recent geochronology of mid to late-Holocene volcanic intrusions (Wright, et al., 2015), however, suggest that there may be unmapped rhyolite bodies that have not been accounted for.

Schmitt and Hulen (2008) estimate that subsidence rates associated with the buried rhyolitic bodies at the SSGF are less than 5 mm yr^{-1}, which is nearly an order of magnitude less than the observed rate. Alternatively, if these bodies were to generate more than 50 mm yr^{-1} at the surface directly overhead by thermal contraction at the documented depths, their effective radii would need to reduce by an amount nearly equivalent to their thickness *each year*, according to a simple volumetric point-source model (Mogi, 1958) with a Poisson's ratio of 0.25 – fulfilling this requirement would produce unphysical strain rates and temperature changes in the rhyolite, assuming a coefficient of thermal expansion of $\sim10^{-5}$ $°C^{-1}$.

There could be cooling of deeper plutonic rock contributing to surface deformation, since the SSGF is located at the apex of an active rift zone, but this source appears to be at depths > 8 km (e.g., Lachenbruch et al., 1985, Hulen et al., 2002) and should not produce short-wavelength, focused subsidence patterns like those in the PS-InSAR data.

3.4 Thermoelastic effects from energy production

Although thermoelastic deformation at the surface might be expected, as energy is harvested from the geothermal reservoir, the data needed to constrain the size of this effect are limited or proprietary. Wellhead temperatures are available, but these are not straightforward representations of reservoir temperature, and cannot be relied upon to assess long-term temporal changes in temperature. Energy production at the SSGF is only a fraction of the geothermal resource potential (Klein et al., 2004), which implies that temperatures would remain relatively stable with relatively constant rates of production from a system with significant vertical permeability structures and vigorous hydrothermal circulation (Norton and Hulen, 2006).

For comparison, deformation at The Geysers Geothermal Field is largely driven by poroelastic stress changes (Mossop and Segall, 1997, 1999) even though the field is steam dominated and has undergone varying rates of reservoir depletion (Sanyal and Enedy, 2011). At the SSGF, thermoelastic deformation would be most apparent at colder-water injection sites (e.g., Kasameyer and Schroeder, 1976; Segall and Fitzgerald, 1998), but this is not obvious in the PS-InSAR data. We performed statistical tests of the mean difference in subsidence rates at both injection and production wells, and do not find evidence of any significant difference between populations.

3.5 Poroelastic effects from energy production

Injection and production data from the SSGF from the DOGGR (Division of Oil, Gas and Geothermal Resources, 2015) indicate that the field has operated under net-production conditions (i.e., production mass rates exceed injection rates) since the majority of active wells were drilled and completed around 1989. This has led some to try and establish a connection between production volumes and seismicity rate changes using stochastic models (e.g., Brodsky and Lajoie, 2013), but the data at hand may not be sufficient to establish a causative relationship, and an observed correlation may be due to a complex set of physical interactions (e.g., Segall and Liu, 2015; Trugman et al., 2016).

We hypothesize that poroelastic contraction is the most likely mechanism to explain focused subsidence in this region. That is – as fluid-mass is removed from the reservoir, the interplay between volumetric strain changes and pore-fluid pressure is large compared to thermal stresses. For an approximately constant rate of extraction and insufficient reinjection and natural recharge to make up for these fluid losses, this interaction predicts an overall decrease in pore pressure over time, with subsidence at the surface resulting from volumetric contraction that is concentrated at reservoir depths. The spatial pattern in deformation at the free surface will be axially symmetric if the dimensions of the source are much smaller than the depth (e.g., Segall, 1985).

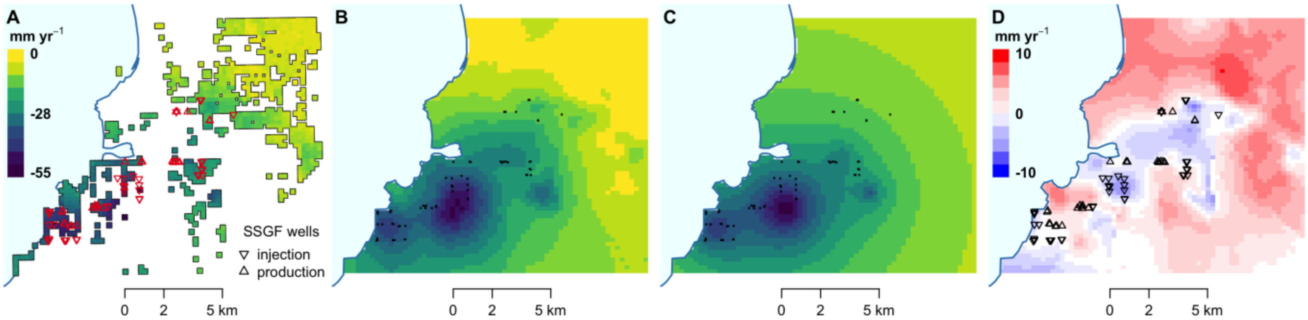

Figure 3: Observed, kriged, and modeled subsidence at the SSGF. (A) Vertical velocities from Envisat PS-InSAR (2003-2010) with locations of active injection and production wells (see Section 2). (B) Interpolated velocity field from a cross-validated, empirical Bayesian kriging method, with coseismic deformation rates removed. (C) Best-fitting velocity field based on four nuclei of strain in a poroelastic halfspace (e.g., Segall, 1985). (D) Residual velocity field (the kriged field minus the modeled field) with locations of active injection and production wells. All velocities are in units of mm yr^{-1}. Map projections are UTM-11N.

Here we test the poroelastic hypothesis by considering multiple volumetric sources, meant to represent differing characteristics of the reservoir (Hulen et al., 2002, 2003) and possible shallow effects unrelated to production. We use the same material property assumptions used as in *Barbour et al.* (2016), specifically a Skempton's coefficient of 0.9 and a fluid density of 950 kg m^3, and modify our inversion scheme to include three additional sources in the model domain. The locations of the additional sources are chosen based on residual anomalies from the single-source model in *Barbour et al.* (2016), at the location of the largest anomaly. Each source is represented by a source depth and mass loss rate (called strength, below), which is solved for by inversion. We solve the non-linear inverse problem using the Levenberg-Marquart (LM) method applied to the PS-InSAR velocities corrected for coseismic moment release. The LM method is a damped iterative procedure that minimizes the sum of the squared error between the data and the model. The best fitting velocity field is shown in Figure 3, with a residual standard error of 3.0 mm yr^{-1}, which is on the order of the median uncertainty in the kriged velocity estimates.

4. DISCUSSION

Although the results shown in Figure 3 are a good representation of the observed velocity field, there are a few important issues to consider when interpreting these results. First, the choice of source locations is based on peaks in the anomaly field, which is somewhat arbitrary; but this is a more defensible approach than *Trugman et al.* (2014) take in fitting surface deformation at the Cerro Prieto field, where a dense field of point sources is prescribed at a fixed depth (effectively linearizing the problem by ignoring depth effects). Their approach is prone to inversion artifacts (e.g., over-fitting), and is inconsistent with details of the Cerro Prieto field, which show a progressive deepening of isotherms and lithofacies to the northeast (Truesdell and Lippmann, 1990; Truesdell, et al., 1997), for example. Secondly, there is an inherent tradeoff between the strength and depth of each source, and interplay between parameters for each source; this implies that careful analyses of probability are needed to evaluate the resulting parameters.

To address interplay between parameter estimates, we calculate likelihood surfaces and 95% confidence intervals (i.e., Beale, 1960) for each parameter pair. Figure 4 shows these tradeoff surfaces for all combinations of the four mass loss rates, the range representative of the SSGF calculated from monthly injection and production data (Division of Oil, Gas and Geothermal Resources, 2015), and the range from previous results using a single source (i.e., Barbour et al., 2016). As the likelihood contours show, there is a global maximum for sources 1 and 2, which represent the two largest subsidence anomalies. This suggests that a single physical mechanism is responsible for sources 1 and 2, or that they share common fluid pathways (e.g., Kasameyer et al., 1984). We note that source 2 is directly below production at Vonderahe-1 but that no production wells are located at source 1.

Figure 5 shows tradeoff surfaces for all combinations of the four source depths, and the range from previous results using a single source (i.e., Barbour et al., 2016). Here, as for the mass loss rates (Figure 4), a strong global maximum in likelihood space can be seen for sources 1 and 2, but nowhere else. This again suggests that sources 1 and 2 result from the same physical mechanism. Furthermore, because the depth of source 1 – below the largest anomaly – is comparable to the single-source results, we have confidence that there is a mechanism of volumetric depletion focused around 1 km. We note that the completion zone for Vonderahe 1 is roughly between 0.6 km and 1.7 km.

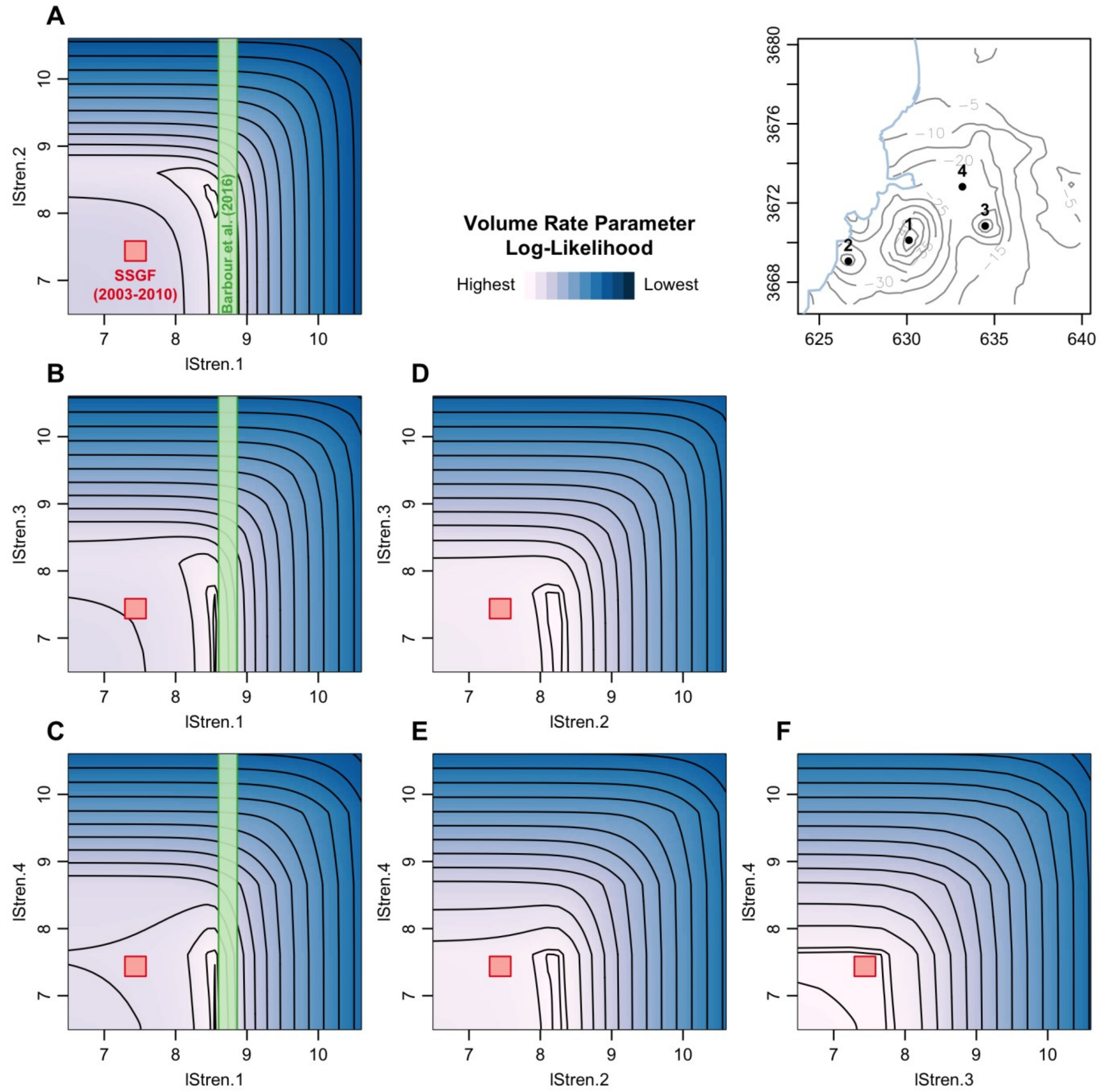

Figure 4: Volume-rate parameter tradeoff. Each frame shows contours of log-likelihood at the given volumetric contraction rate, for each of the four sources in the inversion (see inset map), with the lightest colors representing the highest likelihood: (A) source 1 versus source 2, (B) source 1 versus source 3, (C) source 1 versus source 4, (D) source 2 versus source 3, (E) source 2 versus source 4, (F) source 3 versus source 4. In each frame the red box shows the reported variation at the SSGF, where the sides of the boxes show the range of aggregate net-extraction rates between 2003 and 2010; in (A) – (C) the vertical rectangle shows the 95% confidence interval from *Barbour et al.* (2016). The strengths of source 1 is linked to the strength of source 2, suggesting they are from the same physical mechanism; sources 3 and 4 appear to be independent of each other and of sources 1 and 2. Volume rate units are in log m^3 yr^{-1}.

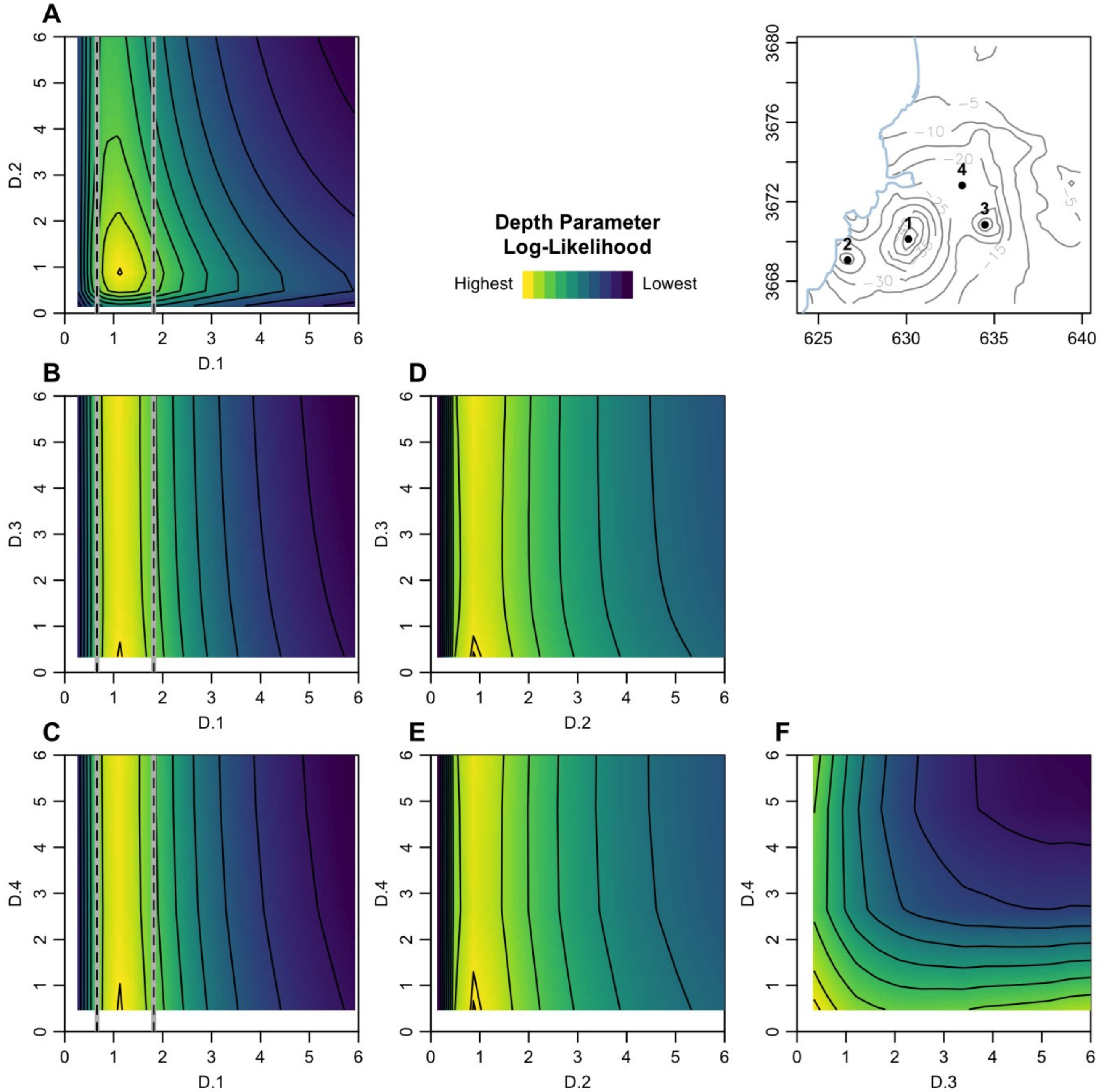

Figure 5: Depth parameter tradeoff. Each frame shows contours of log-likelihood at the given depths of volumetric contraction, for each of the four sources in the inversion (see inset map), with the lightest colors representing the highest likelihood: (A) source 1 versus source 2, (B) source 1 versus source 3, (C) source 1 versus source 4, (D) source 2 versus source 3, (E) source 2 versus source 4, (F) source 3 versus source 4, which has no clear maximum, indicating they represent completely independent mechanisms. In (A) – (C) the vertical dashed lines show the range of 95% confidence intervals from *Barbour et al.* (2016). The depth of source 1 is linked to the depth of source 2, suggesting they are from the same physical mechanism focused at ~1 km; sources 3 and 4 appear to be independent of each other and of sources 1 and 2. Depth units are in km.

4.1 Relation to SSGF operational parameters

Fitting the PS-InSAR data with multiple volumetric sources yields a set of mass-loss estimates that are more than an order of magnitude larger than the reported aggregate annual mass loss for the SSGF, although they are in closer agreement than estimates from a single-source model results. It is not clear why the estimated fluid loss rates are so high, but possibilities include a lack of accounting for tectonic subsidence, compaction, thermoelastic effects, uncertainties in model parameters and assumptions, and errors in measured mass production/injection rates. There is considerable uncertainty associated with the monthly data used to calculate the aggregate rates, because of the difficulties inherent in quantifying flow rates, but these are not expected to be more than ~10% (M. Woods, *personal communication*, 2016).

Furthermore, this parameter discrepancy highlights a severe deficiency in the assumptions used in the base model of surface deformation, where volumetric strain nucleates at a depth greater than the thickness of the reservoir. Specifically, for depletion from a spatially extensive reservoir like the SSGF, with differing characteristics across the field (e.g., Hulen et al., 2002, 2003), a simple point-source model is clearly inappropriate. If there is hydraulic communication occurs across the reservoir, and significant variations in cap rock depth and thickness, these conditions could either attenuate or amplify volumetric strain contributions (e.g., Allis, et al., 2009). At the SSGF, completion zones at production wells are open from the bottom of the casing to the total depth of the well; our models cannot account for this. Furthermore, our models predict subsidence across the entire domain, which is not consistent with the velocity estimates and undoubtedly introduces a bias in best-fitting source parameters. A more realistic modeling approach would consider poroelastic effects from fluid injection and fluid extraction, thermoelastic coupling, fracture compliance and permeability, and permeability changes; all evaluated in a realistic 3-D geo-hydrologic model of the SSGF reservoir – the subject of future investigations.

4.2 Subsidence prior to geothermal production

Considering the style of tectonics associated with the Salton Trough – a transtensional pull-apart basin – it can be expected that some proportion of the observed subsidence is natural, as we have suggested. Geodetic studies prior to geothermal production are limited, but show a broad pattern of subsidence in the Salton Trough attributed to faulting and sediment compaction (e.g., Lofgren, 1979), with highest rates observed near the southern Salton Sea. However, these data are often based on interpolations of large scale leveling surveys, which have large uncertainties, and do not capture the complex spatial pattern revealed by spatially dense PS-InSAR data (i.e., Eneva et al., 2012).

Long-term trends in groundwater level time series have been used to infer horizontal tilt rates (Wilson and Wood, 1980) and vertical motion (Hudnut and Beavan, 1989) in the Salton Trough, but there is generally poor spatial coverage, and the results depend strongly on assumptions of porosity and hydro-mechanical parameters of the rock, which are difficult to verify. But if the tilt rates in *Wilson and Wood* (1980) are representative of pre-production rates, then post-production rates implied by *Eneva et al.* (2012) are more than two times greater than pre-production values at most locations.

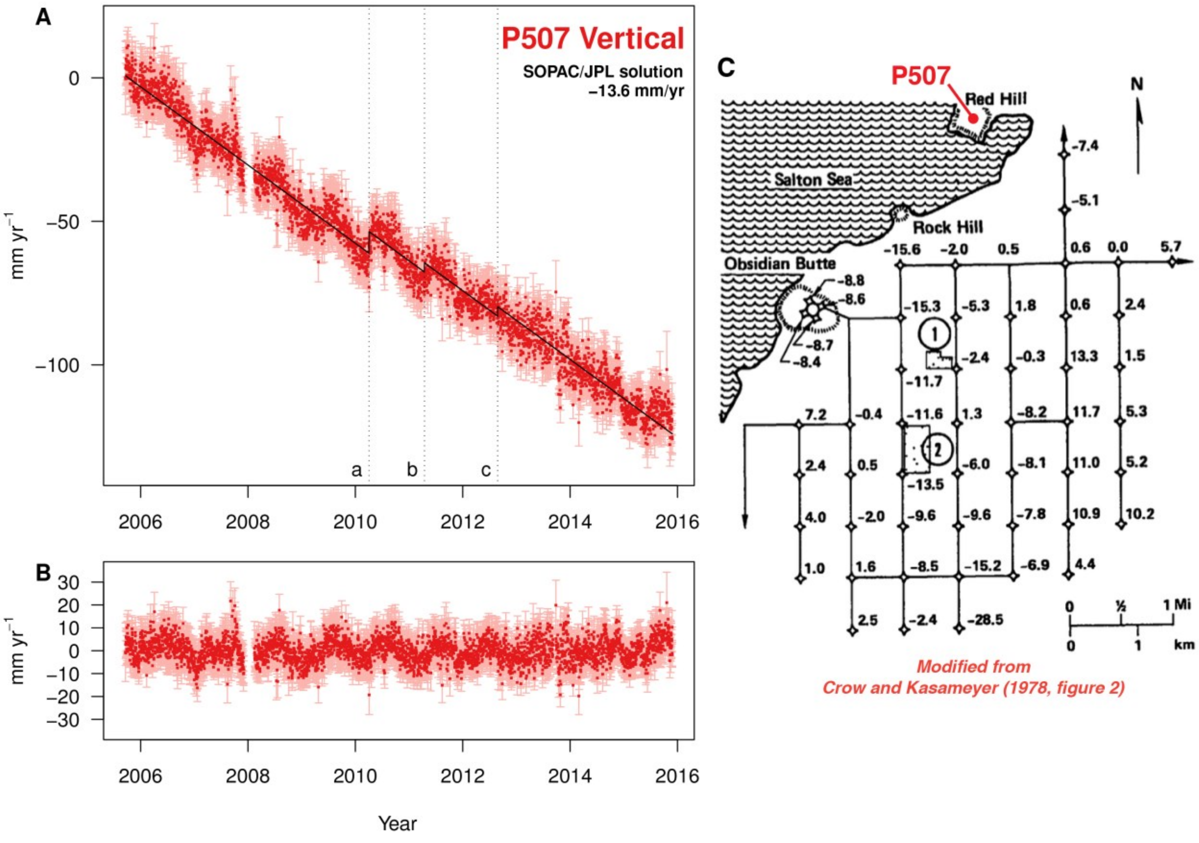

Modified from Crow and Kasameyer (1978, figure 2)

Figure 6: Vertical rates at P507 (Red Hill). A: Timeseries of the combined SOPAC/JPL solution. B: Residual timeseries after removing a long-term trend of -13.6 mm yr^{-1} and coseismic offsets for (a) the 2010 M7.2 El Mayor Cucapah earthquake, (b) a network adjustment, and (c) the 2012 Brawley swarm. C: Map showing the location of P507 compared to leveling data from 1976 to 1977 [modified from Crow and Kasameyer (1978, their figure 2)].

We compare leveling data collected prior to production with modern geodetic data and find marked disagreement: the Red Hill volcanic butte, for example, is subsiding at a rate of 13.6 ± 0.1 mm yr^{-1} based on continuous GPS observations at P507 since late 2005 (Figure 6); whereas, maps from *Lofgren* (1979) suggest nearly three times that rate because of interpolation across a sparse grid of benchmarks. *Crowell et al.* (2013) survey benchmarks emplaced prior to production, finding a similar pattern of broad-scale subsidence; however, because those benchmarks were surveyed only once prior to production, the rates they observe near the Salton Sea and Brawley geothermal fields represent a mixture of natural and anthropogenic signals and cannot be relied upon to assess pre- versus post-production differences. *Crow and Kasameyer* (1978) study the motion of a local array of benchmarks in the SSGF over the span of a year prior to production of the reservoir. They did not survey Red Hill, where P507 is, but the nearest benchmark (~ 1 km to the east, Figure 6C) shows a subsidence rate of 7.4 mm yr^{-1} (no uncertainties are reported), and many benchmarks along the east side of the field show uplift. Indeed a number of benchmarks in *Crow and Kasameyer* (1978) show subsidence, but their spatial pattern resembles a swale focused between uplift features and anti-correlated with the contemporary subsidence field (Figure 7).

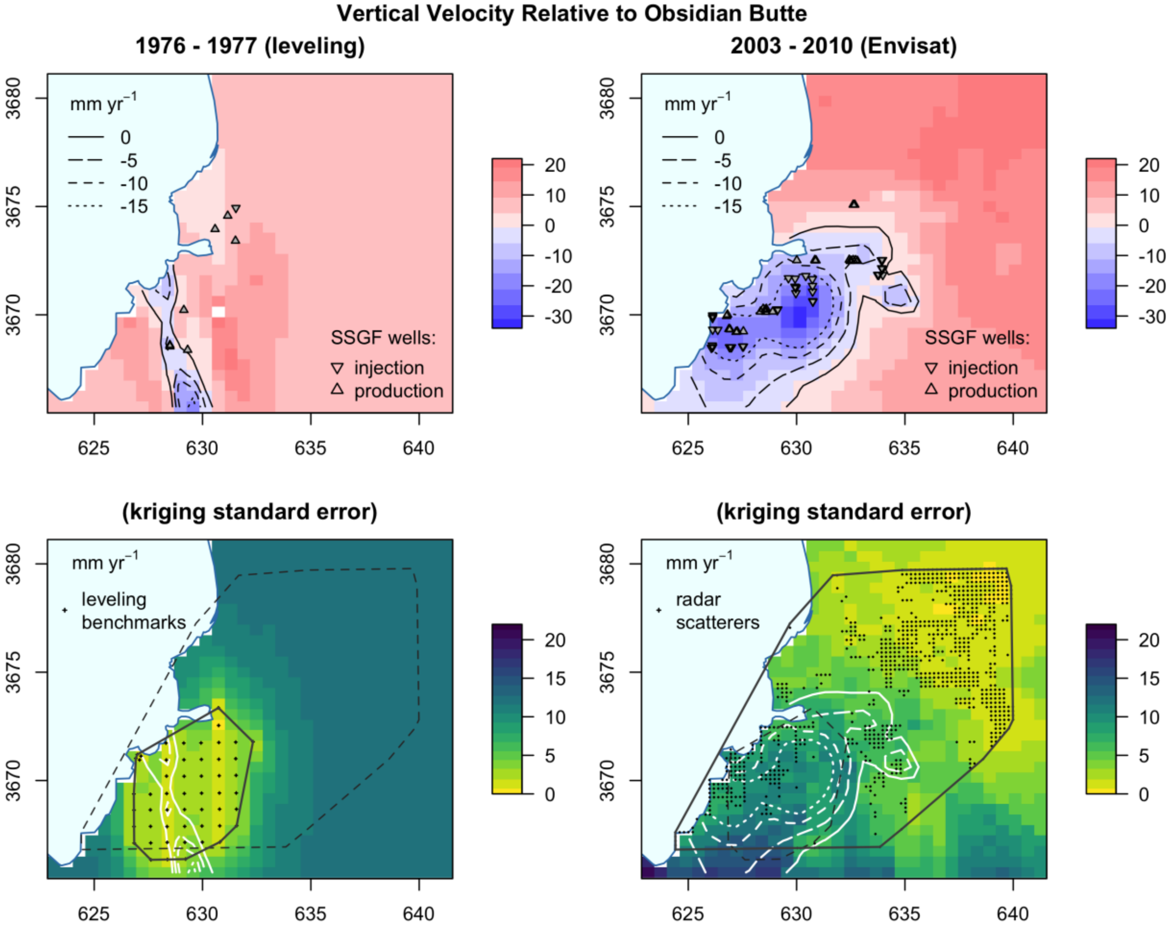

Figure 7: Vertical velocities at the SSGF, relative to rates at Obsidian Butte, before and during production. Left: Velocity field based on leveling data from 1976 to 1977 (Crow and Kasameyer, 1978), prior to major production (which began in 1981 and reached net-production conditions by 1989). Right: Velocity field based on Envisat PS-InSAR data from 2003 to 2010 (Eneva et al., 2012), during major production. Top: Velocity predictions from empirical Bayesian kriging, with contours as noted and locations of SSGF wellheads. Bottom: Uncertainties in the kriged velocities, with velocity contours for reference; the polygons encompass a convex hull around the locations of the original data. Velocities are in mm yr^{-1}. Map projections are UTM-11N.

4.3 Changes in reservoir pressure

Without temporal data on reservoir pressures that can be correlated with observed surface displacements, it is difficult to confirm the nature and magnitude of the poroelastic effect that we suggest is the most significant control on subsidence at the SSGF. Wellhead pressures are publically available, but like the wellhead temperature records these data do not accurately reflect downhole pressures.

Public time series from the Imperial Irrigation District's observation well IID-7 show a pressure decline of ~ 8 psi yr^{-1} (~0.056 MPa yr^{-1}) from 1989 to 1992, sampled at a depth of 244 m – approximately the depth of the reservoir caprock. If the undrained, isothermal volumetric strain associated with this pore pressure change is $\varepsilon = p/B\kappa$ (e.g., Roeloffs, 1996), where B is Skempton's coefficient [about 0.5 for sandstone, independent of differential stress (Lockner and Stanchits, 2002)] and κ is the elastic bulk modulus (about 4.2 GPa from velocity logs at IID-7), then a pore pressure reduction of 8 psi yr^{-1} would induce a 2.6×10^{-5} yr^{-1} contractional strain rate in the rock. [For reference, strain rates at the southern San Andreas Fault, at Durmid Hill, are on the order of 10^{-7} yr^{-1} (Agnew and Wyatt, 2003).] Then, if the main subsidence anomaly, u_Z, is to be explained by a spherical body directly below the anomaly, then the tradeoff between the volume-change and depth of the sphere is $\Delta V \approx 3d^2 u_Z/16 \approx 9.8\, d^2$, assuming an undrained Poisson's modulus of 0.33.

Such volume/depth tradeoff conditions would require either a small volume deforming at shallow depths (< 300 m), or a large volume deforming at much greater depths (>> 300 m). In any case it is unlikely that pressure changes are equivalent across the field, because of the varying thermo-mechanical structure of the reservoir, and varying levels of production across the field. Even though a trend of -8 psi yr^{-1} is seen at IID-7, this was observed more than two decades ago, around the time when net production rates were increasing (with further development of the field to come), and at a depth which may not be an adequate representation of pressure across the completion zone. Perhaps the effects of cumulative mass loss are likely stronger now, and contemporary pressure changes in the reservoir are substantially different. Ideally this supposition could be tested with data from the deep observation wells.

5. CONCLUSION

Using non-linear inversions we find that the most likely mechanism explaining the high rates of subsidence at the SSGF is the ongoing fluid-mass loss associated with produced fluids from geothermal field operations. Parameters from two sources in our model, representing the largest subsidence anomalies, are linked to each other in likelihood space; these are focused at depths comparable to completion zones at production wells in the SSGF. The difference between the expected deformation from fluid extraction at the reported rates and our best-fitting model parameters is too large to attribute to uncertainties in the reported flow-rates or inaccurate assumptions of material properties, and might be due to plasticity effects that a poroelastic model cannot account for. However, the spatial patterns of subsidence clearly resemble that calculated for this set of mass-loss sources. This finding does not preclude the effects of natural sources manifesting in surface deformation, but we suggest that natural sources are not as significant in comparison to anthropogenic sources. Indeed, tectonic features (i.e., active faults) that compartmentalize the geothermal reservoir may be influenced by extraction-related stress changes, but because point-source models are clearly unrealistic, our findings warrant a detailed geomechanical investigation involving borehole fluid pressure monitoring, numerical simulations, and (where available) detailed information on reservoir geometry and physical properties.

ACKNOWLEDGEMENTS

This paper benefited from internal reviews by Andrea Llenos and Martin Schoenball. AJB and ELE acknowledge support from the USGS Mendenhall Fellowship program. Any use of trade, firm, or product names is for descriptive purposes only and does not imply endorsement by the U.S. Government.

REFERENCES

Agnew, D. C., and F. K. Wyatt: Long-base laser strainmeters: A review, *SIO Technical Report*, Scripps Institution of Oceanography, La Jolla, California, http://repositories.cdlib.org/sio/techreport/2/, 2003.

Allis, R., C. Bromley, and S. Currie: Update on subsidence at the Wairakei–Tauhara geothermal system, New Zealand, *Geothermics*, **38** (1), pp. 169-180, 2009.

Barbour, A. J., E. L. Evans, S. H. Hickman, and M. Eneva: Subsidence Rates at the Southern Salton Sea Consistent with Reservoir Depletion, *in review*, 2016.

Beale, E. M. L.: Confidence regions in non-linear estimation, *Journal of the Royal Statistical Society, Series B (Methodological)*, pp. 41–88, 1960.

Brodsky, E. E., and L. J. Lajoie: Anthropogenic Seismicity Rates and Operational Parameters at the Salton Sea Geothermal Field, *Science*, **341** (6145), pp. 543–546, doi:10.1126/science.1239213, 2013.

Brothers, D. S., N. W. Driscoll, G. M. Kent, A. J. Harding, J. M. Babcock, and R. L. Baskin: Tectonic evolution of the Salton Sea inferred from seismic reflection data, *Nature Geoscience*, **2** (8), pp. 581–584, doi:10.1038/ngeo590, 2009.

Brothers, D. S., D. Kilb, K. Luttrell, N. Driscoll, and G. Kent: Loading of the San Andreas fault by flood-induced rupture of faults beneath the Salton Sea, *Nature Geoscience*, **4** (7), pp. 486–492, doi:10.1038/ngeo1184, 2011.

Crow, N. B., and P. W. Kasamayer: Monitoring Natural Subsidence and Seismicity in the Imperial Valley as a Basis for Evaluating Potential Impacts of Geothermal Production, *Transactions of the Geothermal Resources Council*, **2**, pp. 125-128, 1978.

Crowell, B. W., Y. Bock, D. T. Sandwell, and Y. Fialko: Geodetic investigation into the deformation of the Salton Trough, *Journal of Geophysical Research: Solid Earth*, **118** (9), pp. 5030–5039, doi:10.1002/jgrb.50347, 2013.

Division of Oil, Gas and Geothermal Resources: Online database, available at ftp://ftp.consrv.ca.gov/pub/oil/geothermal, last accessed December 2015.

Eneva, M., D. Adams, G. Falorni, and J. Morgan: Surface deformation in Imperial Valley, CA, from satellite radar interferometry, *Geothermal Resources Council Transactions*, **36**, pp. 1339–1344, 2012.

Geertsma, J., Land subsidence above compacting oil and gas reservoirs, *J. Pet. Tech.*, **25** (6), pp. 734-744, doi:10.2118/3730-PA, 1973.

Hudnut, K. W., and J. Beavan: Vertical deformation (1952–1987) in the Salton Trough, California, from water level recordings, *Journal of Geophysical Research: Solid Earth*, **94** (B7), pp. 9463–9476, doi:10.1029/JB094iB07p09463, 1989.

Hulen, J., and F.S. Pulka: Newly-discovered, ancient extrusive rhyolite in the Salton Sea geothermal field, Imperial Valley, California, *Proceedings, Twenty-Sixth Workshop on Geothermal Reservoir Engineering SGP-TR-168, Stanford University, Stanford*, pp. 1-16, 2001.

Hulen, J. B., D. Kaspereit, D. L. Norton, W. Osborn, F. S. Pulka, and R. Bloomquist: Refined conceptual modeling and a new resource estimate for the Salton Sea geothermal field, Imperial Valley, California, *Transactions of the Geothermal Resources Council*, **27**, pp. 29-36, 2002.

Hulen, J., D. Norton, D. Kaspereit, L. Murray, T. van de Putte, and M. Wright: Geology and a working conceptual model of the Obsidian Butte (Unit 6) sector of the Salton Sea Geothermal Field, California, *Transactions of the Geothermal Resources Council*, **27**, pp. 227-240, 2003.

Kasameyer, P. W. and R. C. Schroeder: Application of thermal depletion model to geothermal reservoirs with fracture and pore permeability, *Proceedings of The Second Workshop on Geothermal Reservoir Engineering*, Stanford, CA, pp. 290-298, 1976.

Kasameyer, P. W., Younker, L. W., and J. M. Hanson: Development and application of a hydrothermal model for the Salton Sea Geothermal Field, California, *Geological Society of America Bulletin*, **95** (10), pp. 1242-1252, doi:10.1130/0016-7606(1984)95<1242:DAAOAH>2.0.CO;2, 1984.

Klein, C. W., J. W. Lovekin, and S. K. Sanyal: New geothermal site identification and qualification, Tech. Rep. P500-04-051, GeothermEx Inc., 2004.

Lockner, D. A., and S. A. Stanchits: Undrained poroelastic response of sandstones to deviatoric stress change, *Journal of Geophysical Research: Solid Earth*, **107** (B12), 2353, doi:10.1029/2001JB001460, 2002.

Lofgren, B. E.: Measured crustal deformation in Imperial Valley, California, *Geothermics*, **8** (3–4), pp. 267-272, doi:10.1016/0375-6505(79)90050-6, 1979.

Lohman, R. B., and J. J. McGuire: Earthquake swarms driven by aseismic creep in the Salton Trough, California, *Journal of Geophysical Research: Solid Earth*, **112**, doi:10.1029/2006JB004596, 2007.

McGuire, J. J., R. B. Lohman, R. D. Catchings, M. J. Rymer, and M. R. Goldman: Relationships among seismic velocity, metamorphism, seismic and aseismic fault slip in the Salton Sea Geothermal Field region, *Journal of Geophysical Research: Solid Earth*, **120**, pp. 2600-2615, doi:10.1002/2014JB011579, 2015.

Meckel, T. A., U. S. Ten Brink, and S. J. Williams: Sediment compaction rates and subsidence in deltaic plains: numerical constraints and stratigraphic influences, *Basin Research*, **19** (1), pp. 19-31, doi:10.1111/j.1365-2117.2006.00310.x, 2007.

Mogi, K.: Relations between the Eruptions of Various Volcanoes and the Deformations of the Ground Surfaces around them, *Bulletin of the Tokyo Earthquake Research Institute*, **36** (2), pp. 99-134, 1958.

Mossop, A., and P. Segall: Subsidence at The Geysers geothermal field, N. California from a comparison of GPS and leveling surveys, *Geophysical Research Letters*, **24** (14), pp. 1839-1842, 1997.

Mossop, A., and P. Segall: Volume strain within The Geysers geothermal field, *Journal of Geophysical Research: Solid Earth*, **104** (B12), pp. 29113-29131, 1999.

Norton, D., and J. Hulen: Magma-Hydrothermal Activity in the Salton Sea Geothermal Field Imperial County, California, *Transactions of the Geothermal Resources Council*, **30**, pp. 991-998, 2006.

Okada, Y.: Surface deformation due to shear and tensile faults in a half-space, *Bulletin of the Seismological Society of America*, **75**, pp. 1135 – 1154, 1985.

Roeloffs, E.: Poroelastic techniques in the study of earthquake-related hydrologic phenomena, *Advances in Geophysics*, **37**, pp. 135-195, 1996.

Rymer, M.J., Treiman, J.A., Kendrick, K.J., Lienkaemper, J.J., Weldon, R.J., Bilham, R., Wei, M., Fielding, E.J., Hernandez, J.L., Olson, B.P., Irvine, P.J., Knepprath, N., Sickler, R.R., Tong, X., and M.E. Siem: Triggered surface slips in southern California associated with the 2010 El Mayor-Cucapah, Baja California, Mexico, earthquake, *U.S. Geological Survey Open File Report*, 2010-1333, 2011.

Sanyal, S. K., and S. L. Enedy: Fifty Years of Power Generation at The Geysers Geothermal Field, California – The Lessons Learned, *Proceedings of the Workshop on Geothermal Reservoir Engineering*, **36**, pp. 45-53, 2011.

Schmitt, A. K., and J. B. Hulen: Buried rhyolites within the active, high-temperature Salton Sea geothermal system, *Journal of Volcanology and Geothermal Research*, **178** (4), pp. 708–718, doi:10.1016/j.jvolgeores.2008.09.001, 2008.

Segall, P.: Stress and subsidence resulting from subsurface fluid withdrawal in the epicentral region of the 1983 Coalinga Earthquake, *Journal of Geophysical Research: Solid Earth*, **90** (B8), pp. 6801–6816, doi:10.1029/JB090iB08p06801, 1985.

Segall, P., and S. D. Fitzgerald: A note on induced stress changes in hydrocarbon and geothermal reservoirs, *Tectonophysics*, 289 (1-3), pp. 117–128, doi:10.1016/S0040-1951(97)00311-9, 1998.

Segall, P., and S. Lu: Injection-induced seismicity: Poroelastic and earthquake nucleation effects, *Journal of Geophysical Research: Solid Earth*, **120**, pp. 5082–5103, doi:10.1002/2015JB012060, 2015.

Shearer, P., E. Hauksson, and G. Lin: Southern California Hypocenter Relocation with Waveform Cross-Correlation, Part 2: Results Using Source-Specific Station Terms and Cluster Analysis, *Bulletin of the Seismological Society of America*, **95** (3), pp. 904–915, doi:10.1785/0120040168, 2005.

Truesdell, A. H. and M. J. Lippmann: Interaction of cold-water aquifers with exploited reservoirs of the Cerro Prieto geothermal system, *Transactions of the Geothermal Resources Council*, **14**, pp. 735–741, 1990.

Truesdell, A. H., M. J. Lippmann, and H. Gutiérrez-Puente, Evolution of the Cerro Prieto reservoirs under exploitation, *Transactions of the Geothermal Resources Council*, **21**, pp. 263-269, 1997.

Trugman, D. T., A. A. Borsa, and D. T. Sandwell: Did stresses from the Cerro Prieto Geothermal Field influence the El Mayor-Cucapah rupture sequence?, *Geophysal Research Letters*, **41**, pp. 8767–8774, doi:10.1002/2014GL061959, 2014.

Trugman, D. T., P. M. Shearer, A. A. Borsa, and Y.: A comparison of long-term changes in seismicity at the Geysers, Salton Sea, and Coso geothermal fields, *Journal of Geophysical Research: Solid Earth*, **121**, doi:10.1002/2015JB012510, 2016.

Van De Kamp, P. C.: Holocene Continental Sedimentation in the Salton Basin, California: A Reconnaissance, *Geological Society of America Bulletin*, **84** (3), pp. 827–848, doi:10.1130/ 0016-7606(1973)84⟨827:HCSITS⟩2.0.CO;2, 1973.

Wei, M., and D. Sandwell: Decorrelation of L-Band and C-Band Interferometry Over Vegetated Areas in California, *Geoscience and Remote Sensing, IEEE Transactions on*, **48** (7), pp. 2942- 2952, doi:10.1109/TGRS.2010.2043442, 2010.

Wilson, M. E. and S. H. Wood: Tectonic tilt rates derived from lake-level measurements, Salton Sea, California, *Science*, **207** (4427), pp. 183-186, 1980.

Wright, H. M., J. A. Vazquez, D. E. Champion, A. T. Calvert, M. T. Mangan, M. Stelten, K. M. Cooper, C. Herzig, and A. Schriener Jr.: Episodic Holocene eruption of the Salton Buttes rhyolites, California, from paleomagnetic, U-Th, and Ar/Ar dating, *Geochemistry Geophysics Geosystems*, **16**, pp. 1198–1210, doi:10.1002/2015GC005714, 2015.

Yang, W., E. Hauksson, and P. M. Shearer: Computing a Large Refined Catalog of Focal Mechanisms for Southern California (1981–2010): Temporal Stability of the Style of Faulting, *Bulletin of the Seismological Society of America*, **102** (3), pp. 1179–1194, doi:10.1785/0120110311, 2012.

Younker, L. W., P. W. Kasameyer, and J. D. Tewhey: Geological, geophysical, and thermal characteristics of the Salton Sea Geothermal Field, California, *Journal of Volcanology and Geothermal Research*, **12** (3), pp. 221–258, doi:10.1016/0377-0273(82) 90028-2, 1982.

Zoback, M. D.: *Reservoir Geomechanics*, 449 pp., Cambridge University Press, 2010.